Enhancement of Carrier Mobility in Semiconductor Nanostructures by Carrier Distribution Engineering

Binxi Liang(梁斌熙), Luhao Liu(刘陆豪), Jiachen Tang(唐家晨), Jian Chen(陈健), Yi Shi(施毅)*, and Songlin Li(黎松林)*

School of Electronic Science and Engineering, National Laboratory of Solid-State Microstructures, and Collaborative Innovation Center of Advanced Microstructures, Nanjing University, Nanjing 210023, China

(Received 21 March 2023; accepted manuscript online 10 April 2023)

Two-dimensional (2D) van der Waals semiconductors are appealing for low-power transistors. Here, we show the feasibility in enhancing carrier mobility in 2D semiconductors through engineering the vertical distribution of carriers confined inside ultrathin channels via symmetrizing gate configuration or increasing channel thickness. Through self-consistently solving the Schrödinger–Poisson equations, the shapes of electron envelope functions are extensively investigated by clarifying their relationship with gate configuration, channel thickness, dielectric permittivity, and electron density. The impacts of electron distribution variation on various carrier scattering matrix elements and overall carrier mobility are insightfully clarified. It is found that the carrier mobility can be generally enhanced in the dual-gated configuration due to the centralization of carrier redistribution in the nanometer-thick semiconductor channels and the rate of increase reaches up to 23% in HfO_2 dual-gated 10-layer MoS_2 channels. This finding represents a viable strategy for performance optimization in transistors consisting of 2D semiconductors.

DOI: 10.1088/0256-307X/40/5/058503

The isolation of graphene and relevant two-dimensional (2D) van der Waals semiconductors has stimulated exploration of their applications in low-power field-effect transistors (FETs) for more-Moore electronics[1–4] and in driving units for high-resolution displays.[5–7] In addition to the merit of atomic thickness that is favorable for enhancing gate electrostatic control,[8–11] the self-saturated surfacial atomic structure represents another important advantage superior to silicon for attaining high device performance by suppressing extrinsic charge scattering events.[11–14] Even though 2D semiconductor FETs have been widely investigated,[15–19] pertinent physical studies regarding the impacts of device parameters and gate configuration on the fundamental envelope function $\Psi(z)$, which determines the distribution of electrons in the ultrathin channels of 2D FETs, or on the carrier mobility remained insufficient.

For 2D FETs, there are various surface-associated carrier scattering mechanisms sensitive to vertical electron distribution inside ultrathin channels.[20–23] Thus, an accurate description of $\Psi(z)$ and its variation with external modulations are essential to reliably calculate the electron scattering rates and overall device performance. For electrically gated bulk Si FETs, the energy bands of the conduction channels bend down at the Si–SiO_2 interface, where the electrically induced 2D electrons are confined within nanometers ranges,[24] forming an approximately 10-nm-thick inversion layer. The empirical $\Psi(z)$ of 2D electrons in the FET inversion layer was first proposed by Fang and Howard,[25] which works well for bulk semiconductors but is invalid for ultrathin 2D van der Waals materials. For this reason, Kim *et al.* fell back on basic physical principles to calculate $\Psi(z)$ in the 2D semiconductors through self-consistent Schrödinger–Poisson solutions,[26] and in the samples that are thicker than 20 nm, they derived a distribution similar to bulk silicon. For semiconductors even thinner or atomically thin, most researchers, for simplification, assumed a centrosymmetric electron distribution in calculation by adopting a form of trigonometric or delta function.[22,27,28] However, such an assumption ignores the lopsided shape of electron distribution that originates from the asymmetrically electric gating in single-gated configuration,[26,29] which may result in large calculation inaccuracy. To improve it, we proposed an empirical method to deal with the lopsidedness in electron distribution in atomically thin MoS_2.[29] Notwithstanding, further researches are still desired to address accurate electron distribution within semiconductors from basic physical principles, in particular in the dimensionality crossover regime from 2D to bulk, and, more importantly, to clarify its impacts on macroscopic device performance.

In this work, we perform a systematic study on the $\Psi(z)$ variation within the dimensionality-crossed MoS_2 channels ranging from 1 to 10 layers by self-consistently solving the 1D Schrödinger–Poisson equations[30] with modulating multiple parameters, including channel thickness t, relative permittivity ε_r of channel, electron density n_s, and gate configuration (single- or dual-gated, SG or DG). The calculation shows that, for SG channels, the peak of electron distribution shifts closer to dielectric-channel interface with increasing vertical gating electric field (determined by n_s and ε_r) or with decreasing t, before channels entering strong inversion (high n_s) or shirking to atomic thickness. The electron distribution under the DG configuration with symmetric gate dielectrics is also inves-

*Corresponding authors. Email: sli@nju.edu.cn; yshi@nju.edu.cn
© 2023 Chinese Physical Society and IOP Publishing Ltd

tigated, featuring symmetric $\Psi(z)$ forms with one or two peaks (dependent on t).

Based on the accurate electron distribution from the Schrödinger–Poisson solutions, the impacts of electron distribution variation on the quantum screening effect among electrons are further studied. Also, we investigate the dependence of individual scattering mechanisms [interfacial Coulomb impurities (CIs), surface optical (SO) phonons, and lattice vacancies] on channel thickness in units of the number of layers (NL) and on overall carrier mobilities at a typical n_s level $\sim 10^{13}\,\mathrm{cm}^{-2}$ for MoS_2 channels encapsulated in hexagonal boron nitride (BN) and HfO_2. By comparing the mobility values under the SG and DG configurations, we uncover the possibility in enhancing carrier mobility through engineering the carrier distribution via symmetrizing gate configuration in channels thicker than 3 nm, where the rate of increase reaches up to 23% in HfO_2 dual-gated 10-layer channels.

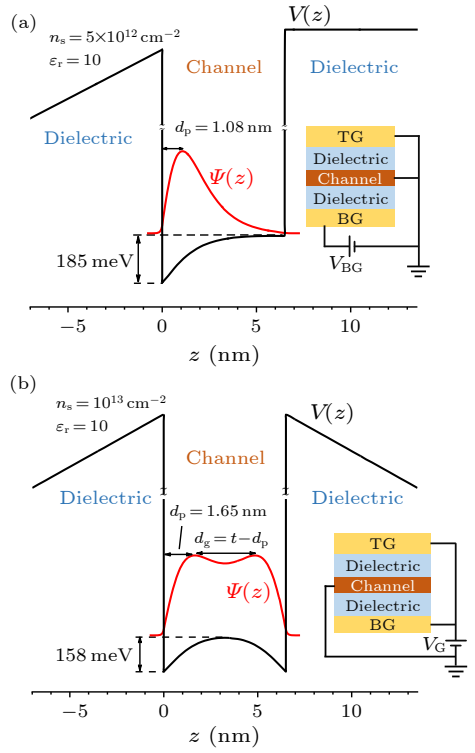

Fig. 1. Band diagram $V(z)$ and electron envelope function $\Psi(z)$ (a) for a bottom-gated channel with $n_s = 5 \times 10^{12}\,\mathrm{cm}^{-2}$ and (b) for a dual-gated channel with $n_s = 10^{13}\,\mathrm{cm}^{-2}$. For the two channels, $t = 6.5$ nm and $\varepsilon_r = 10$. Insets show the corresponding gate configurations.

Methods and Discussion. To look insight into the effect of gate configuration, we first study $\Psi(z)$ in a 6.5-nm-thick (10 layers) MoS_2 channel under varied SG and DG configurations, where the channel is encapsulated by two 10-nm-thick dielectrics with ε_r of 10. Both the dielectrics are covered with metallic gates. Figure 1(a) shows $\Psi(z)$ of channel electrons at $n_s = 5 \times 10^{12}\,\mathrm{cm}^{-2}$ and corresponding potential profile $V(z)$ of the device under the SG configuration. In such a configuration, the channel and top gate (TG) are electrically grounded while the bottom gate (BG) is biased with a positive voltage V_{BG}, as shown in the inset. In comparison with the flat band exhibited by the top dielectric, the band of the gated channel shows a downward bending of 185 meV near the bottom interface, resulting in an electric field of 0.9 MV/cm. Because of the attraction of gate electric field to induced electrons, $\Psi(z)$ is lopsidedly distributed toward the side of BG. To describe such a lopsided distribution, a quantity d_p is introduced to characterize the distance from the distribution peak to the gating dielectric interface. A low d_p value of 1.08 nm is estimated under the SG configuration, indicating the tight coupling and strong interaction between the channel electrons with the dielectric interface.

For comparison, Fig. 1(b) shows $\Psi(z)$ and $V(z)$ under the DG configuration. Here an equivalent-field principle is adopted to compare the electron distributions in channels under the two gate configurations. Hence, a gate voltage of the same magnitude is additionally applied to TG and thus n_s reaches $10^{13}\,\mathrm{cm}^{-2}$, twice the level under the SG configuration. Because the device and biasing conditions become strictly symmetric, $\Psi(z)$ and $V(z)$ are both symmetrized accordingly. The band bending at the channel interfaces is reduced to 158 meV, slightly lower than that in the SG configuration, with its energy maximum located at the center. Likewise, the envelope function becomes centrosymmetric, in spite of the two peaks caused by the electrostatic effect from the dual gates. In this case, d_p is increased to 1.65 nm, indicating the higher possibilities for electrons to occupy the middle region of the channel. As a result, the electrons are more immune to the scattering events at the channel/dielectric interfaces, constituting the rationale for mobility enhancement.

Apart from gate configuration, t, ε_r, and n_s are also interesting parameters that affect electron distribution. We then study the dependence of d_p on n_s and ε_r in channels with different t values of 6.5 nm (10 layers) and 0.65 nm (monolayer). The results are plotted in Fig. 2(a). Under the SG configuration, the general tendency for both channels is that d_p decreases with increasing n_s or decreasing ε_r, which is attributed to the reinforcement of the surface electric field given by the equation, $E = en_s/(\varepsilon_0\varepsilon_r)$, where e is the elementary charge and ε_0 is the vacuum dielectric constant. Nevertheless, the rates of variation in the two channels are different, where the dependence of d_p on n_s and ε_r are more prominent in the thick one. For instance, at $n_s = 10^{13}\,\mathrm{cm}^{-2}$, d_p is 1.14 nm when $\varepsilon_r = 12$ but decreases to 0.7 nm when $\varepsilon_r = 3$. Also, the variation rate of d_p by n_s is quite high, reaching $\sim 60\%$ for $\varepsilon_r = 3$. By contrast, d_p variation is rather small in the thin channel and d_p is almost unchanged as n_s or ε_r changes [bottom panel, Fig. 2(a)]. In the parametric ranges covered, it varies by 3% at most, suggesting that the electron distribution in the monolayer channels is less adjustable because of the spatial confinement effect.

Figure 2(b) shows the contour plot for d_p versus t (0.65–6.5 nm) and ε_r (2–13) at a fixed high n_s of $10^{13}\,\mathrm{cm}^{-2}$ under the SG configuration. Three distinct regions (t-dependent, ε_r-dependent, and saturated) are seen in the plot, as divided by the dashed lines. In the t-dependent region, d_p increases monotonically with increasing t because of the weakening of spatial confinement. Such t-dependent behavior occurs in low-t range and persists no more than

4 nm even at high ε_r, while it shifts to ε_r-dependent when t is large enough. In the ε_r-dependent region, d_p is insensitive to t but highly depends on ε_r, varying mainly with the vertical gating electric field. In the saturated region where ε_r and t are simultaneously high, electron distribution is almost independent of these two parameters and thus becomes almost unadjustable. The above observation is a natural consequence of the Schrödinger–Poisson equations, which include the two coexisting quantum and electrostatic mechanisms that govern the distribution of electrons in channels. In thick channels, the electrons are primarily confined by the band bending caused by the electrostatic gating, while in thin channels, the electrons are squeezed within narrow spaces and the spatial confinement effect becomes dominant.

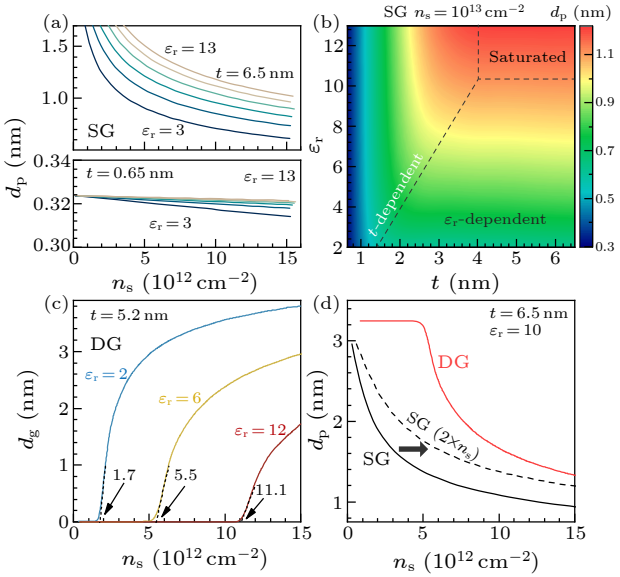

Fig. 2. (a) Comparison of the dependence of d_p on n_s between 6.5 and 0.65 nm SG channels with various ε_r in the ranging from 3 to 13 with steps of 2. (b) Contour plot for d_p versus t and ε_r at $n_s = 10^{13}$ cm^{-2}. (c) Comparison of the dependence of d_g on n_s in a 5.2-nm-thick DG channel with $\varepsilon_r = 2$, 6, 12. (d) Comparison of the dependence of d_p on n_s in channels under varied gate configurations. Solid red and black lines denote the cases of DG and SG configurations, respectively. Dashed black line represents the result for an SG channel under the equivalent-field principle (i.e., $V_{SG} = V_{BG}$), which leads to a doubled n_s.

Technologically speaking, DG FETs can exhibit stronger electrostatic control capacity and feature higher downscaling ability than the SG counterparts.[31] Thus, it is important to contrastively study the electron distributions in the DG channels, in particular in thickness of few nanometers. As shown in Fig. 1(b), $\Psi(z)$ is centrosymmetric in the DG channels due to symmetrized $V(z)$, and thus it would exhibit one or two distribution peaks, depending on t. To focus on this feature, here we choose another quantity d_g to describe the gap between the two separated peaks, which is given by $d_g = t - 2d_p$. Note that d_g would be reduced to zero in thin channels or under weak electrostatic modulation where the two peaks evolve into an overlapped one, and thus $d_p = t/2$ if $d_g = 0$ (i.e., single peak).

Figure 2(c) presents the dependence of d_g on n_s for a 5.2-nm-thick (8 layers) DG MoS_2 channel with different ε_r values of 2, 6, and 12. In the low n_s regime where the channel is insufficiently gated, only one overlapped peak appears in the electron distribution and results in $d_g = 0$. However, when n_s increases to some threshold values (dependent on ε_r), two distribution peaks would arise and lead to a nonzero d_g that increases with increasing n_s. The threshold values are 1.7, 5.4, and 11.1×10^{12} cm^{-2} for devices with $\varepsilon_r = 2$, 6, and 12, respectively. The corresponding surface electric fields amount to 0.79, 0.82, and 0.84 MV/cm, respectively, suggesting the trend of a high surface electric field required at large ε_r to divide the electron distribution into two peaks.

To understand the impact of gate configuration on $\Psi(z)$, in Fig. 2(d) we compare d_p between the DG and SG channels with $t = 6.5$ nm (10 layers) and $\varepsilon_r = 10$ in an n_s range from 0 to 1.5×10^{13} cm^{-2}. At the same n_s levels (i.e., $V_{SG} = 2V_{DG}$), d_p in the BG channel is generally smaller than that in the DG channel (see the solid black and red lines). Such a trend holds even under the constant-field principle by setting $V_{SG} = V_{DG}$ (i.e., $n_{DG} = 2n_{SG}$). For clarity, the solid black line in Fig. 2(d) is translated into the dashed black line by taking n_s as $2n_s$, i.e., the parameter on the horizontal axis for the dashed line should be $2n_s$ when keeping the values 0, 5, 10, 15 unchanged. The generally reduced d_p behavior under the DG working configuration is a consequence of the symmetrized electrostatic interaction by gate fields, further confirming the potential immunity for electrons to extrinsic scatterings from interfaces under the DG configuration.

It is well known that quantum screening arises mainly from the electron–electron interaction and behaves as a modulation on response to external electric fields by electron gases in solids.[24,28] In principle, any changes in external stimuli would cause variation in the average distance between electrons and result in polarization of the dense electron gases confined in the ultrathin channels. Considering that the problem of permittivity mismatch between channels and dielectrics has been well studied,[22,28,29,32] for the sake of simplicity we temporarily assume that the MoS_2 channels are encapsulated in two dielectric layers with the same ε_r as MoS_2. Such a dielectric environment without permittivity mismatch greatly simplifies the calculation on scattering matrix elements but preserves the effect of electron distribution variation.

To further shed light on the impacts of electron distribution on carrier scattering, we next study the dependence of quantum screening (i.e., electron–electron interaction) and individual scattering mechanisms on t, n_s, and gate configuration in nanoscale MoS_2 channels. Among the various scattering mechanisms including interfacial CIs,[29] SO phonon,[22,33] surface roughness,[13] and lattice defects,[16] the former two are sensitive to electron distribution. Thus, we focus on the impacts of electron distribution on these two mechanisms.

The dielectric function of electron gas is given by the well-known Lindhard formula[24,34]

$$\varepsilon_{2d}(q,T) = 1 + \frac{e^2}{2\varepsilon_0\varepsilon_r q} F_{ee}(q)\Pi(q,T), \tag{1}$$

where q is the scattering wave vector of the 2D electrons, $\Pi(q,T)$ is the polarizability function at temperature T, and $F_{\rm ee}$ is the form factor given by

$$F_{\rm ee}(q) = \int_0^t \int_0^t \Psi(z_1)^2 \Psi(z_2)^2 \exp(-q|z_1 - z_2|) dz_1 dz_2. \quad (2)$$

Figure 3(a) shows the dependence of $F_{\rm ee}(k_{\rm F})$ on t in SG and DG MoS_2 at $n_{\rm s} = 10^{13}\,{\rm cm}^{-2}$, where $k_{\rm F}$ is the Fermi wave vector. According to Eq. (2), one can find that $F_{\rm ee}$ is strongly associated with the compactness of electron distribution (i.e., average distance between electrons). In the extremely compact case with an ideal delta distribution we have $F_{\rm ee} = 1$, while $F_{\rm ee}$ is less than 1 in less compact distributions. In practical cases, the monolayer MoS_2 ($t = 0.65\,{\rm nm}$) has the most compact distribution among all thicknesses, and thus, shows the highest $F_{\rm ee}$ value of 0.88. Generally, $F_{\rm ee}$ decreases monotonically with increasing t because of the broadening of electron distribution. However, the rates of decay are different between SG and DG configurations. Under the SG configuration, $F_{\rm ee}$ reaches saturation of 0.65 at $t \approx 5\,{\rm nm}$, while it shows no sign of saturation up to 6.5 nm under the DG configuration. Moreover, $F_{\rm ee}$ under the DG configuration is always smaller than that under the SG configuration, because electrons are generally dispersed in the former case. The inset of Fig. 3(a) also shows the dependence of $F_{\rm ee}$ on q for a 6.5 nm channel. In general, $F_{\rm ee}$ decreases monotonically with q, and it decreases faster under the DG configuration than that under the SG one.

As mentioned above, the variation of $n_{\rm s}$ will also result in the change of average distance between electrons and overall screening effect, we then study the dependence of $F_{\rm ee}$ on $n_{\rm s}$ at an example $q = 0.5\,{\rm nm}^{-1}$ for a 6.5 nm MoS_2, as shown in Fig. 3(b). Interestingly, $F_{\rm ee}$ of the SG channel increases monotonically with increasing $n_{\rm s}$ in the range of 10^{12}–$10^{13}\,{\rm cm}^{-2}$, while it shows an opposite trend in the DG channel, resulting from the less compact electron distribution in channel under the DG configuration.

For 2D semiconductors, the scattering from interfacial CIs, which originates from dangling bands and chemical residues at channel surfaces, constitutes an important limiting factor for carrier mobility.[29] Hence, we study the effects of variation of electron distribution on its intensity. The scattering matrix element of interfacial CI scattering is given by

$$M_q^{\rm CI} = \frac{e^2}{2S\varepsilon_0\varepsilon_{\rm r} q} \frac{F_{\rm ec}(q)}{\varepsilon_{\rm 2d}(q)}, \quad (3)$$

where S is the area of channel, $F_{\rm ec}$ is the coupling factor used to evaluate the Coulomb interaction between channel electrons and interfacial CIs. Considering the lopsided distribution of SG channels, $F_{\rm ec}$ contains two terms: $F_{\rm ec}^{\rm BCI}$ and $F_{\rm ec}^{\rm TCI}$, which account for the interaction of electrons to the CIs located at the bottom and top interfaces, respectively.[20,29] For the DG channels, the two terms are the same because of the symmetrized electron distributions.

Likewise, we also calculate the dependence of the two $F_{\rm ec}$ terms on t and q, as shown in Fig. 3(c), which intentionally separates the contributions from the top and bottom interfaces under the SG configuration. All these terms decrease monotonically with t, because the interaction distances between electrons and interfacial CIs (scaling roughly with $d_{\rm p}$ and $t - d_{\rm p}$) increase with increasing t. Still assuming that the SG channel is bottom gated, we find that $F_{\rm ec}^{\rm BCI}$ saturates to $\sim$0.47 around $t \approx 5\,{\rm nm}$ due to the saturation of $d_{\rm p}$. By contrast, $F_{\rm ec}^{\rm TCI}$ keeps decreasing till $t = 6.5\,{\rm nm}$, because the distance between electrons and top interfacial CIs (i.e., $t - d_{\rm p}$) will not saturate with increasing t, which renders the scattering from the top interfacial CIs negligible in thick channels. $F_{\rm ec}$ under the DG configuration is smaller than $F_{\rm ec}^{\rm BCI}$ but larger than $F_{\rm ec}^{\rm TCI}$ under the SG counterpart because $d_{\rm p}$ in the former case is always in the middle of the latter two cases.

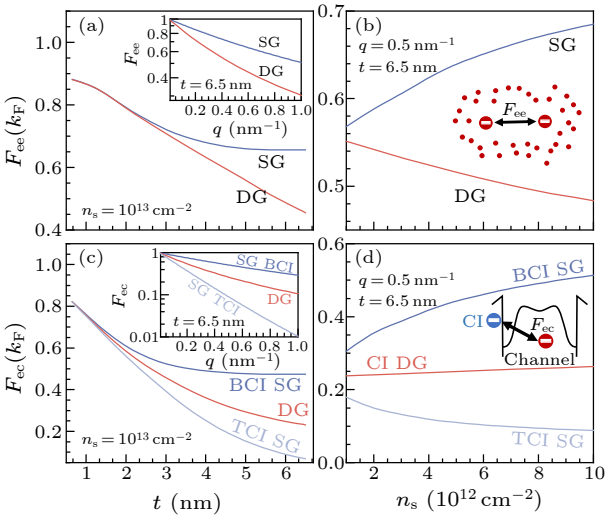

Fig. 3. [(a), (b)] Dependence of quantum screening term $F_{\rm ee}$ for SG and DG MoS_2 (a) on t at $q = k_{\rm F}$ and $n_{\rm s} = 10^{13}\,{\rm cm}^{-2}$, and (b) on $n_{\rm s}$ at $q = 0.5\,{\rm nm}^{-1}$ and $t = 6.5\,{\rm nm}$. Inset in (a) shows the dependence of $F_{\rm ee}$ on q for DG and SG MoS_2 with $t = 6.5\,{\rm nm}$ and $n_{\rm s} = 10^{13}\,{\rm cm}^{-2}$. Inset in (b) shows the schematic diagram for screened Coulomb interaction between two channel electrons confined in the background of electron sea in the channel. The impacts from gate configuration are also shown. [(c), (d)] Corresponding plots for the $F_{\rm ec}$ terms due to Coulomb coupling between channel electrons and CIs. The device parameters are adopted as the same as those in (a) and (b). Inset in (d) shows the schematic origin for the $F_{\rm ec}$ terms.

The inset in Fig. 3(c) shows the q dependence of the three $F_{\rm ec}$ terms for a 6.5-nm-thick MoS_2 at $n_{\rm s} = 10^{13}\,{\rm cm}^{-2}$. All the terms sharply decay with increasing q, roughly following an exponential law, $F_{\rm ec} = \exp(-qd_{\rm eq})$, where $d_{\rm eq}$ is an equivalent distance between interfacial CIs and channel electrons that are projected to obey an ideal delta distribution. For the SG channel with $n_{\rm s} = 10^{13}\,{\rm cm}^{-2}$, the $d_{\rm eq}$ for the bottom (top) interface is about 0.53 nm (2.0 nm). For the DG channel, the $d_{\rm eq}$ is estimated to be 0.96 nm. This result can be used as a fast approximation to calculate the complicated $F_{\rm ec}$ terms.[20,29] Also, Fig. 3(d) shows dependence of $F_{\rm ec}$ terms on $n_{\rm s}$ at the example q of $0.5\,{\rm nm}^{-1}$. Under the DG configuration, $F_{\rm ec}$ is weakly dependent on $n_{\rm s}$, which only increases from 0.24 to 0.26 in a wide $n_{\rm s}$ range from 10^{12} to $10^{13}\,{\rm cm}^{-2}$. By contrast, the increasing or decreasing trend of the $F_{\rm ec}^{\rm BCI}$

or $F_{\rm ec}^{\rm TCI}$ term is more appreciable under the SG configuration, resulting from the dramatic variation of the lopsided electron distribution in the SG channels.

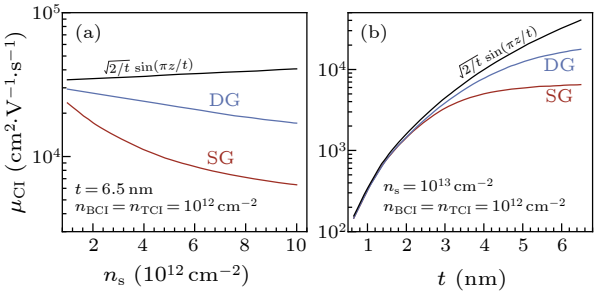

Fig. 4. (a) Calculated dependence of $\mu_{\rm CI}$ on $n_{\rm s}$ for SG and DG MoS_2 channels with accurate and conventional trigonometric electron distributions. Channel thickness is set to 6.5 nm. (b) Relevant dependence of $\mu_{\rm CI}$ on t at $n_{\rm s} = 10^{13}\,{\rm cm}^{-2}$.

After understanding the impacts of device parameters (t and $n_{\rm s}$) and gate configuration on crucial terms $\Psi(z)$, $F_{\rm ee}$ and $F_{\rm ec}$, we further look into insight into their influence on the CI-limited mobility ($\mu_{\rm CI}$). By assuming a same CI density of $10^{12}\,{\rm cm}^{-2}$ at the top and bottom interfaces in a 6.5-nm MoS_2 channel,[20] we calculated $\mu_{\rm CI}$ under the two gate configurations on the basis of the accurate electron distributions from the Schrödinger–Poisson solutions, as shown by the red and blue lines in Fig. 4(a). In both the cases, $\mu_{\rm CI}$ decreases with increasing $n_{\rm s}$. Such a descending trend is mainly attributed to the negative correlation between $d_{\rm p}$ and $n_{\rm s}$ [Fig. 2(d)], which can increase the Coulomb interaction between channel electrons and interfacial CIs. In addition, the values of $\mu_{\rm CI}$ under the SG configuration are much smaller than those under the DG configuration, because of the generally smaller $d_{\rm p}$ at a fixed $n_{\rm s}$ under the former case.

For comparison with the conventional trigonometric approximation on $\Psi(z)$, we also calculate the relevant $\mu_{\rm CI}$–$n_{\rm s}$ curve [black line in Fig. 4(a)], which exhibits a slightly ascending trend with $n_{\rm s}$. Such an ascending trend is an overall consequence due to the enhancement of quantum screening and the increase of Fermi level as $n_{\rm s}$ increases. However, it contradicts with the calculations with realistic electron distributions, indicating the presence of large deviation in calculating electronic performance of thick channels by using the conventional trigonometric $\Psi(z)$.

In Fig. 4(b), we further clarify the inconsistency induced by inappropriate use of $\Psi(z)$ through fully calculating the $\mu_{\rm CI}$–t curves for the accurate and trigonometric electron distributions. In all the cases, the $\mu_{\rm CI}$–t trends are consistent. However, the $\mu_{\rm CI}$ curves based on the accurate distributions saturate more easily in thick channels due to the fast saturation of electron distribution, while the curve based on the trigonometric distribution shows no sign to saturate. Noticeably, the $\mu_{\rm CI}$ would be generally overestimated in channels thicker than 3 nm and the overestimation reaches up to an intolerable level of 3 folds at $t > 5$ nm when calculated from the approximation of trigonometric distribution. Hence, the trigonometric approximation is acceptable only for channels below 3 nm, representing useful guidance for device modeling.

It has been reported that the scattering from SO phonons in high-k dielectrics represents another significant interfacial scattering mechanism relevant to carrier mobility.[21,33] The scattering matrix element of SO phonon scattering can be written as[33,35]

$$M_q^{\rm SO} = \frac{F_{\rm SO}(q)}{\varepsilon_{\rm 2d}(q)}\sqrt{\frac{e^2 E_{\rm SO}}{2Sq\varepsilon_0}\left(\frac{1}{\varepsilon_{\rm ox}^{\infty}+\varepsilon_{\rm r}^{\infty}}-\frac{1}{\varepsilon_{\rm ox}^{0}+\varepsilon_{\rm r}^{\infty}}\right)}, \quad (4)$$

where $E_{\rm SO}$ is the energy of SO phonon, $\varepsilon_{\rm ox}^{\infty}$ ($\varepsilon_{\rm ox}^{0}$) is the optical (static) permittivity of the dielectric, and $F_{\rm SO}$ is the coupling factor for the interaction between electrons and SO phonons. Likewise, we use $F_{\rm SO}^{\rm BCI}$ and $F_{\rm SO}^{\rm TCI}$ to denote the SO phonon scattering from the bottom and top dielectrics, respectively.[22,24,36]

In addition to interfacial CIs and SO phonons, structural defects (DFs) in MoS_2 lattice could be a third important type of leading scattering mechanism.[23,37] Although there are many categories of structural defects in MoS_2, the lattice vacancies due to the loss of sulfur atoms at channel surfaces are believed to be the dominant one present in high-quality samples.[38,39] Normally, the lattice vacancies are treated as short-range scattering mechanism;[16,29] thus we assume that the lattice vacancies are mainly distributed in the surfacial layers of MoS_2 by adopting a delta approximation for the scattering potential as $eL_{\rm B}^2/(\varepsilon_0\varepsilon_{\rm r})\delta(x,y,z-z_0)$, where $L_{\rm B}$ is the length of Mo-S bond. As such, the scattering matrix element is derived as

$$M_q^{\rm DF} = \frac{e^2 L_{\rm B}^2 \Psi(z_0)^2}{\varepsilon_{\rm 2d}(q)\varepsilon_0\varepsilon_{\rm r} S}. \quad (5)$$

Finally, we calculate the dependence of room-temperature mobility on channel thickness in units of NL under different gate configurations and with varied dielectrics based on the accurate electron distributions. For accuracy, the mismatched dielectric environments are strictly considered in our calculation.[22,40] Figure 5 shows the mobilities of BN- and HfO_2-encapsulated MoS_2 under the SG and DG configurations as a function of NL. The leading scattering sources are also plotted individually, including intrinsic phonons, CIs, SO phonons, and DFs. In the case of BN dielectric [Fig. 5(a)], the component of SO phonons is neglected because it is too weak to be considered.[22,41] The CI densities ($n_{\rm CI}$) at the bottom and top interfaces are assumed to be identical with $n_{\rm CI} = 2\times10^{11}\,{\rm cm}^{-2}$ for BN[42] and $10^{12}\,{\rm cm}^{-2}$ for HfO_2, respectively. The densities of defects ($n_{\rm DF}$) are assumed to be $10^{13}\,{\rm cm}^{-2}$ at both channel surfaces.[37,38] The intrinsic mobility ($\mu_{\rm int}$) from lattice phonons is adopted from pervious prediction,[43] having an NL-independent value of $410\,{\rm cm}^2\cdot{\rm V}^{-1}\cdot{\rm s}^{-1}$ at room temperature. The total mobilities are estimated with Matthiessen's rule.

Two important pieces of information for performance optimization can be seen from Fig. 5. First, μ increases with NL because the CI, DF, and SO limited mobilities all show positive correlation with NL, resulting from the generally large interaction distance $d_{\rm p}$ between electrons and surface scattering sources. From the viewpoint of mobility only, the channels with thickness of a few layers are more appropriate than monolayers for more-Moore electronics,

despite the extraordinary immunity of monolayers to the short-channel effect. For applications in driving transistors where the downscaling is not so urgent, slightly thick DG channels (>5 layers) are more favorable.

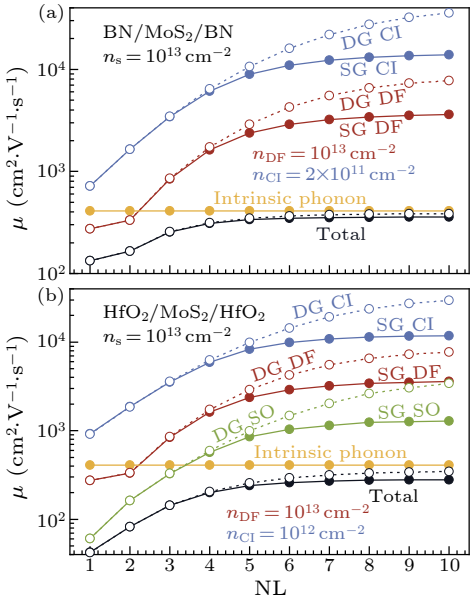

Fig. 5. Calculated individual μ components and overall values versus the number of layers (NL) at room temperature with $n_s = 10^{13}\,\mathrm{cm}^{-2}$ for various scattering mechanisms including CIs, DFs, lattice phonons, and SO phonons in (a) BN-encapsulated MoS_2 and (b) HfO_2-encapsulated MoS_2.

Second, μ components under the DG configuration are generally higher than those under the SG one for all the three surface associated mechanisms, which is also associated with the variation in compactness of electron distribution due to symmetrized electrostatic gating under the DG configuration. Though the difference in mobility is inappreciable between the DG and SG configuration when NL < 5, it quickly increases in thicker channels with NL > 5. In the case of HfO_2 encapsulated FETs, gate configuration can bring about 23% enhancement in overall mobility at NL $= 10$. Therefore, we propose that the carrier mobility in nanoscale semiconductors can be effectively enhanced through appropriately engineering the carrier distributions in channels via optimizing thickness and gate configuration.

It is noteworthy that the above results are calculated for high-quality devices because all the parameters of the extrinsic scattering sources are adopted at low levels, where the impacts of electron distribution variation are minimized because the electron distribution irrelevant lattice phonons act as the primary factor limiting mobility in the regime of thick channels. For most practical devices, the levels of CIs and DFs can be even higher in 1–2 orders of magnitude and they likely serve as the dominant scattering sources. The enhancement rates of mobility through the carrier distribution engineering can be even higher under such circumstances.

In summary, we have provided a deep insight into the relationship of electron distributions with multiple factors including gate configuration, channel thickness, dielectric permittivity, and electron density, by virtue of self-consistent solutions from the 1D Schrödinger–Poisson equations. Also, we have clarified its impacts on various carrier scattering matrix elements and overall carrier mobility based on the Boltzmann transport equation. Importantly, we show the possibility in enhancing carrier mobility in 2D semiconductors through engineering the vertical distribution of carriers confined inside the ultrathin channels via symmetrizing gate configuration or increasing channel thickness. The rate of enhancement reaches up to 23% in HfO_2 dual-gated clean MoS_2 channels. These systematic results provide useful guidance for device design and performance optimization in developing ultrathin transistors for advanced electronics.

Acknowledgements. This work was supported by the National Key R&D Program of China (Grant Nos. 2022YFA1203802 and 2021YFA1202903), the National Natural Science Foundation of China (Grant Nos. 92264202, 61974060, and 61674080), and the Innovation and Entrepreneurship Program of Jiangsu Province.

References

[1] Shen P C, Su C, Lin Y, Chou A S, Cheng C C, Park J H, Chiu M H, Lu A Y, Tang H L, Tavakoli M M, Pitner G, Ji X, Cai Z, Mao N, Wang J, Tung V, Li J, Bokor J, Zettl A, Wu C I, Palacios T, Li L J, and Kong J 2021 *Nature* **593** 211
[2] Desai S B, Madhvapathy S R, Sachid A B, Llinas J P, Wang Q, Ahn G H, Pitner G, Kim M J, Bokor J, Hu C, Wong H S P, and Javey A 2016 *Science* **354** 99
[3] Akinwande D, Huyghebaert C, Wang C H, Serna M I, Goossens S, Li L J, Wong H S P, and Koppens F H 2019 *Nature* **573** 507
[4] Quhe R, Xu L, Liu S, Yang C, Wang Y, Li H, Yang J, Li Q, Shi B, Li Y, Pan Y, Sun X, Li J, Weng M, Zhang H, Guo Y, Xu L, Tang H, Dong J, Yang J, Zhang Z, Lei M, Pan F, and Lu J 2021 *Phys. Rep.* **938** 1
[5] Meng W Q, Xu F F, Yu Z H, Tao T, Shao L G, Liu L W, Li T T, Wen K C, Wang J P, He L B, Sun L, Li W, Ning H, Dai N, Qin F, Tu X, Pan D, He S, Li D, Zheng Y, Lu Y, Liu B, Zhang R, Shi Y, and Wang X 2021 *Nat. Nanotechnol.* **16** 1231
[6] Shin J, Kim H, Sundaram S, Jeong J, Park B I, Chang C S, Choi J, Kim T, Saravanapavanantham M, Lu K, Kim S, Suh J M, Kim K S, Song M K, Liu Y, Qiao K, Kim J H, Kim Y, Kang J H, Kim J, Lee D, Lee J, Kim J S, Lee H E, Yeon H, Kum H S, Bae S H, Bulovic V, Yu K J, Lee K, Chung K, Hong Y J, Ougazzaden A, and Kim J 2023 *Nature* **614** 81
[7] Hwangbo S, Hu L, Hoang A T, Choi J Y, and Ahn J H 2022 *Nat. Nanotechnol.* **17** 500
[8] Ieong M, Doris B, Kedzierski J, Rim K, and Yang M 2004 *Science* **306** 2057
[9] Yan R H, Ourmazd A, and Lee K 1992 *IEEE Trans. Electron. Dev.* **39** 1704
[10] Hisamoto D, Kaga T, Kawamoto Y, and Takeda E 1989 *IEEE International Electron Devices Meeting* (Washington, DC, USA) pp 833–836
[11] He X, Fronheiser J, Zhao P, Hu Z, Uppal S, Wu X, Hu Y, Sporer R, Qin L, Krishnan R, Bazizi E M, Carter R, Tabakman K, Jha A K, Yu H, Hu O, Choi D, Lee J G, Samavedam S B, and Sohn D K 2017 *IEEE International Electron Devices Meeting* (2–6 December 2017, San Francisco, CA) pp 2021–2024
[12] Bhoir M S, Chiarella T, R L Å, Mitard J, Terzeiva V, Horiguchi N, and Mohapatra N R 2019 *IEEE J. Electron. Devices Soc.* **7** 1217

[13] Jin S, Fischetti M, and Tang T W 2007 *IEEE Trans. Electron. Devices* **54** 2191
[14] Gomez L, Aberg I, and Hoyt J L 2007 *IEEE Electron. Device Lett.* **28** 285
[15] Fiori G, Bonaccorso F, Iannaccone G, Palacios T, Neumaier D, Seabaugh A, Banerjee S K, and Colombo L 2014 *Nat. Nanotechnol.* **9** 768
[16] Cui X, Lee G H, Kim Y D, Arefe G, Huang P Y, Lee C H, Chenet D A, Zhang X, Wang L, Ye F, Pizzocchero F, Jessen B S, Watanabe K, Taniguchi T, Muller D A, Low T, Kim P, and Hone J 2015 *Nat. Nanotechnol.* **10** 534
[17] Radisavljevic B and Kis A 2013 *Nat. Mater.* **12** 815
[18] Chhowalla M, Jena D, and Zhang H 2016 *Nat. Rev. Mater.* **1** 16052
[19] Liu Y, Duan X, Shin H J, Park S, Huang Y, and Duan X 2021 *Nature* **591** 43
[20] Ju S H, Liang B X, Zhou J, Pan D F, Shi Y, and Li S L 2022 *Nano Lett.* **22** 6671
[21] Zeng L, Xin Z, Chen S, Du G, Kang J, and Liu X 2013 *Appl. Phys. Lett.* **103** 113505
[22] Ma N and Jena D 2014 *Phys. Rev. X* **4** 011043
[23] Li S L, Tsukagoshi K, Orgiu E, and Samori P 2016 *Chem. Soc. Rev.* **45** 118
[24] Ando T, Fowler A B, and Stern F 1982 *Rev. Mod. Phys.* **54** 437
[25] Fang F and Howard W 1966 *Phys. Rev. Lett.* **16** 797
[26] Kim S, Konar A, Hwang W S, Lee J H, Lee J, Yang J, Jung C, Kim H, Yoo J B, Choi J Y, Jin Y W, Lee S Y, Jena D, Choi W, and Kim K 2012 *Nat. Commun.* **3** 1011
[27] Jena D and Konar A 2007 *Phys. Rev. Lett.* **98** 136805
[28] Ong Z Y and Fischetti M V 2013 *Phys. Rev. B* **88** 165316
[29] Li S L, Wakabayashi K, Xu Y, Nakaharai S, Komatsu K, Li W W, Lin Y F, Aparecido-Ferreira A, and Tsukagoshi K 2013 *Nano Lett.* **13** 3546
[30] Stern F 1970 *J. Comput. Phys.* **6** 56
[31] Colinge J P 2008 *FinFETs and Other Multi-Gate Transistors* (Boston, MA: Springer)
[32] Trolle M L, Pedersen T G, and Véniard V 2017 *Sci. Rep.* **7** 39844
[33] Fischetti M V, Neumayer D A, and Cartier E A 2001 *J. Appl. Phys.* **90** 4587
[34] Maldague P F 1978 *Surf. Sci.* **73** 296
[35] Wang S Q and Mahan G D 1972 *Phys. Rev. B* **6** 4517
[36] Konar A, Fang T, and Jena D 2010 *Phys. Rev. B* **82** 115452
[37] Yu Z H, Pan Y M, Shen Y T, Wang Z L, Ong Z Y, Xu T, Xin R, Pan L, Wang B, Sun L, Wang J, Zhang G, Zhang Y W, Shi Y, and Wang X 2014 *Nat. Commun.* **5** 5290
[38] Hong J H, Hu Z X, Probert M, Li K, Lv D H, Yang X, Gu L, Mao N, Feng Q, Xie L, Zhang J, Wu D, Zhang Z, Jin C, Ji W, Zhang X, Yuan J, and Zhang Z 2015 *Nat. Commun.* **6** 6293
[39] Zhou W, Zou X, Najmaei S, Liu Z, Shi Y, Kong J, Lou J, Ajayan P M, Yakobson B I, and Idrobo J C 2013 *Nano Lett.* **13** 2615
[40] Kumar A and Ahluwalia P 2012 *Physica B* **407** 4627
[41] Perebeinos V and Avouris P 2010 *Phys. Rev. B* **81** 195442
[42] Liang B X, Wang A J, Zhou J, Ju S H, Chen J, Watanabe K, Taniguchi T, Shi Y, and Li S 2022 *ACS Appl. Mater. Interfaces* **14** 18697
[43] Kaasbjerg K, Thygesen K S, and Jacobsen K W 2012 *Phys. Rev. B* **85** 115317